

Supporting Information

Multimodal Image Fusion Offer Better Spatial Resolution for Mass Spectrometry Imaging

Lei Guo ^a, Jinyu Zhu ^a, Keqi Wang ^b, Kian-Kai Cheng ^c, Jingjing Xu ^a, Liheng Dong ^d, Xiangnan Xu ^e,
Can Chen ^f, Mudassir Shah ^a, Zhangxiao Peng ^g, Jianing Wang ^h, Zongwei Cai ^h, Jiyang Dong ^{a,*}

^a Department of Electronic Science, National Institute for Data Science in Health and Medicine, Xiamen University, Xiamen 361005, China

^b Institute of Big Data Science and Industry, Shanxi University, Taiyuan 030006, China

^c Faculty of Chemical and Energy Engineering, Universiti Teknologi Malaysia, Johor Bahru, Johor 81310, Malaysia

^d School of Computing and Data Science, Xiamen University Malaysia, Sepang 43600, Malaysia

^e School of Mathematics and Statistics, The University of Sydney, Sydney, NSW 2006, Australia

^f Department of Hepatobiliary Surgery and Fujian Institute of Hepatobiliary Surgery, Fujian Medical University Union Hospital, Fuzhou 350001, China

^g Department of Molecular Oncology, Eastern Hepatobiliary Surgery Hospital & National Centre for Liver Cancer, Navy Military Medical University, Shanghai 200438, China

^h State Key Laboratory of Environmental and Biological Analysis, Department of Chemistry, Hong Kong Baptist University, Hong Kong SAR 999077, China

This supplementary file includes:

1. Supplementary Tables

| | |
|---|----|
| Table S1. Public datasets analyzed in this paper | S3 |
|---|----|

2. Supplementary Figures

| | |
|--|-----|
| Figure S1. The original low-resolution ion images and the corresponding high-resolution reconstruction image using DeepFERE model. | S4 |
| Figure S2. Prediction results of DeepFERE for the masked region. | S5 |
| Figure S3. Data fusion of low-dimensional representation of a human colorectal adenocarcinoma cancer MSI data and the corresponding H&E image for high-resolution reconstruction. | S6 |
| Figure S4. Registration results of different methods. | S7 |
| Figure S5. The results of ablation study. | S8 |
| Figure S6. Errors backpropagation diagram of DeepFERE. | S9 |
| Figure S7. The calculation of \mathcal{L}_{cor} . | S10 |
| Figure S8. DeepFERE models for enhancing embedding data and single ion image. | S11 |

3. Supplementary Materials

| | |
|--|-----|
| Material S1. UMAP dimension reduction | S12 |
| Material S2. Detailed of comparison methods | S13 |
| Material S3. Detailed of Ablation study | S14 |
| Material S4. Potential solution to address overfitting. | S15 |
| Material S5. Detailed of MSI data preprocessing | S16 |
| Material S6. Detailed of Quantitative evaluation | S17 |
| References | S18 |

Table S1. Public datasets analyzed in this paper

| Tissue | Data Source | Detailed of MSI or ST dataset | Detailed of H&E image |
|---------------------------------|---|---|---|
| Mouse Brain | Plas <i>et al.</i> ¹ (http://fusion.vueinnovations.com/) | 40×36 pixels with 795 m/z features, measured at 100 μ m resolution | 815×656 pixels with 3 RGB features, measured at 5 μ m |
| Human colorectal adenocarcinoma | Glen <i>et al.</i> ² (https://www.ebi.ac.uk/metabolights/MTBLS415) | 59×67 pixels with 391 m/z features, measured at 100 μ m resolution | 213×388 pixels with 3 RGB features, measured at 25 μ m |
| Mouse Brain | 10x Genomics (https://support.10xgenomics.com/spatial-gene-expression/datasets/) | 27 × 30 pixels with 19456 gene features, measured at 100 μ m resolution | 540 × 600 pixels with 3 RGB features, measured at 5 μ m |

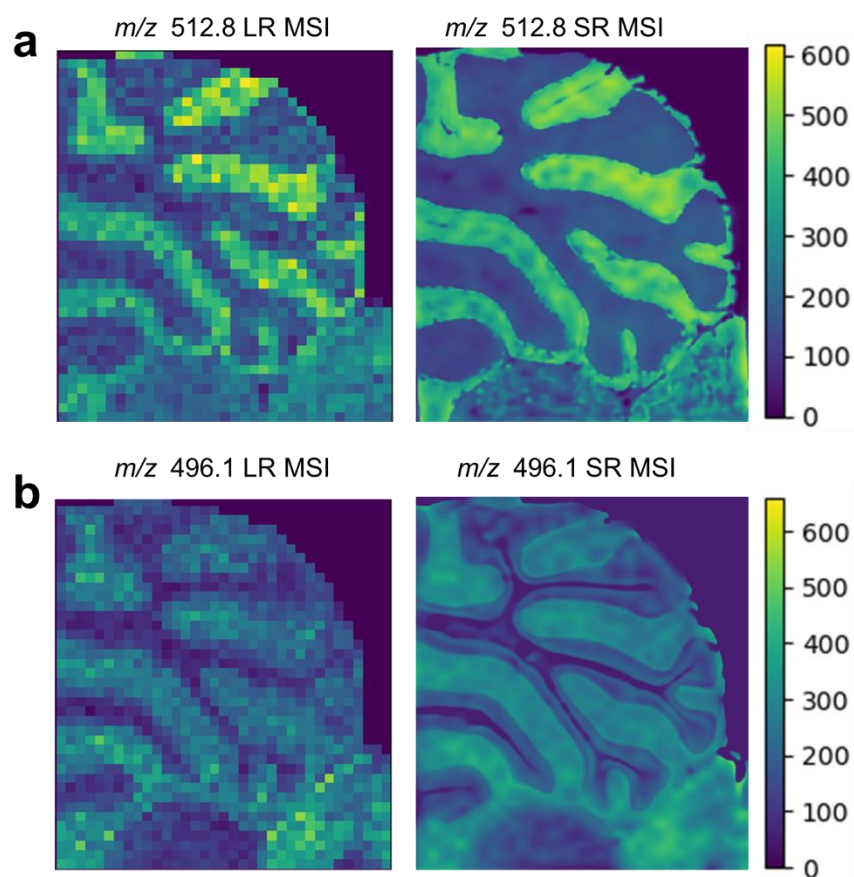


Figure S1. The original low-resolution ion images and the corresponding high-solution reconstruction image using DeepFERE model. (a) ion image m/z 512.8; (b) ion image m/z 496.1.

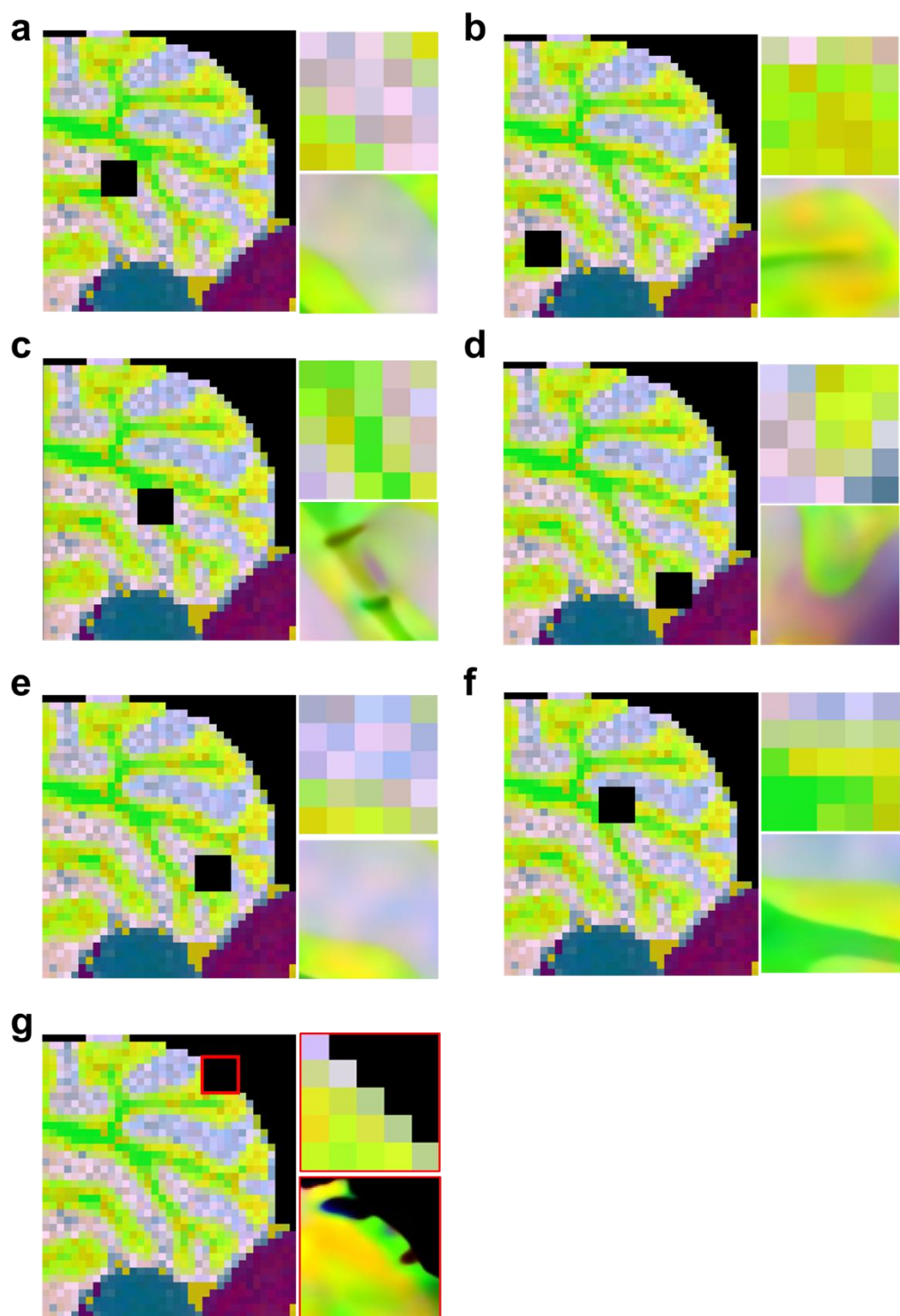


Figure S2. Prediction results of DeepFERE for the masked region. (a-g) where the top right is the masked region, and the bottom right is the predicted region.

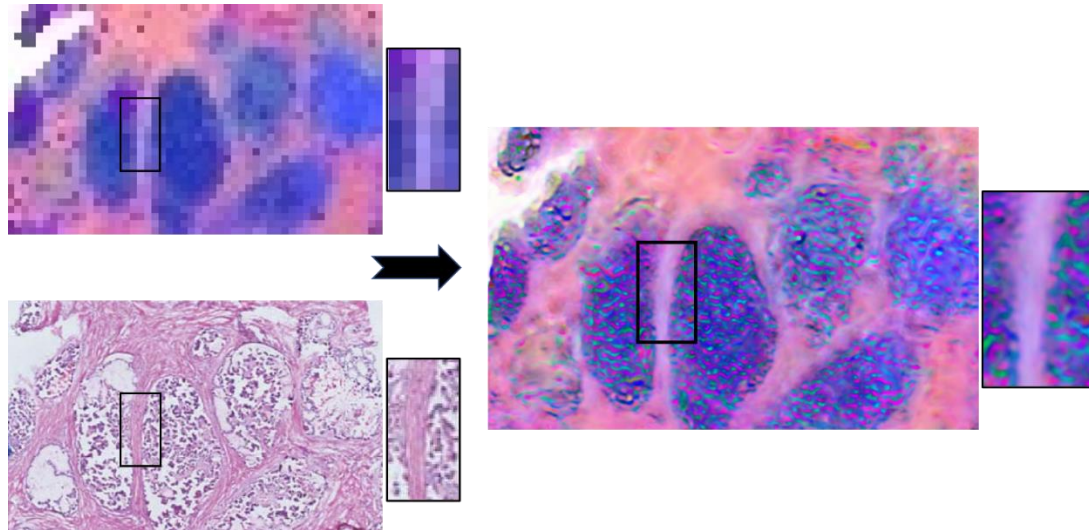


Figure S3. Data fusion of low-dimensional representation of a human colorectal adenocarcinoma cancer MSI data and the corresponding H&E image for high-resolution reconstruction.

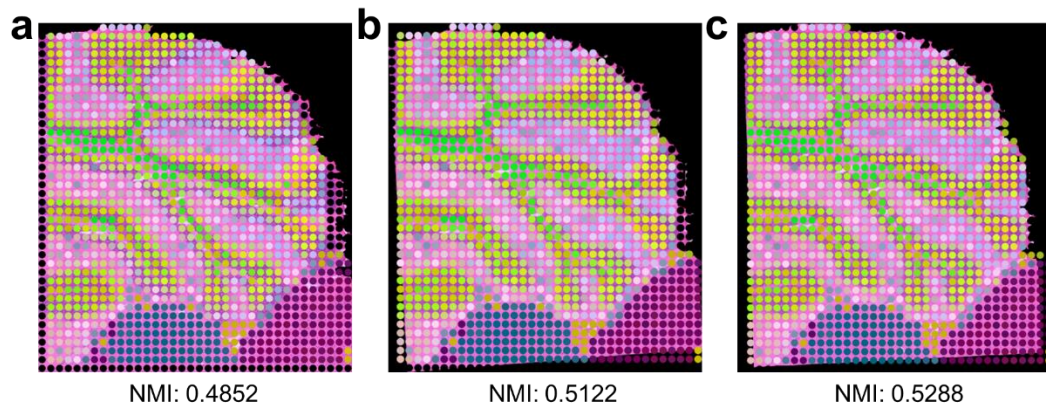


Figure S4. Registration results of different methods. (a) The original H&E image, (b) Manual registration using “cpselect()” and “cp2tform()” functions in MATLAB, (c) Automatic registered H&E image (the current method). The highest normalization mutual information (NMI) value was achieved by the current proposed method suggesting the best registration performance of our method.

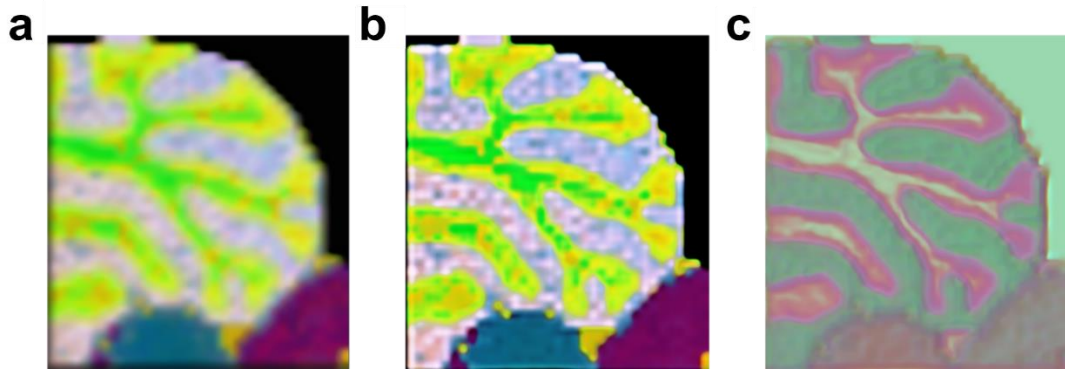


Figure S5. The results of ablation study. (a) Remove the loss function of L_{pre} ; (b) Remove the loss function of L_{cor} ; (c) Remove the loss function of L_{rec} .

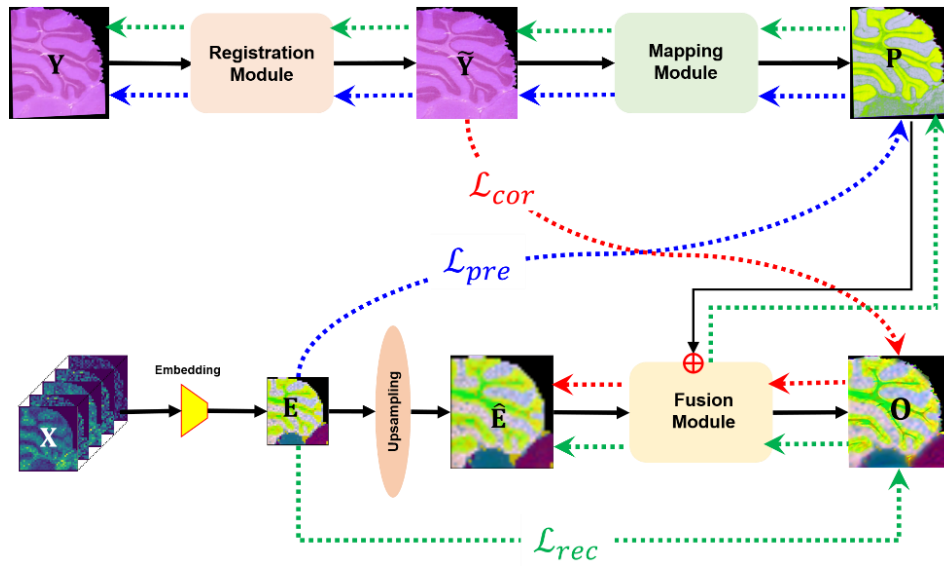


Figure S6. Errors backpropagation diagram of DeepFERE.

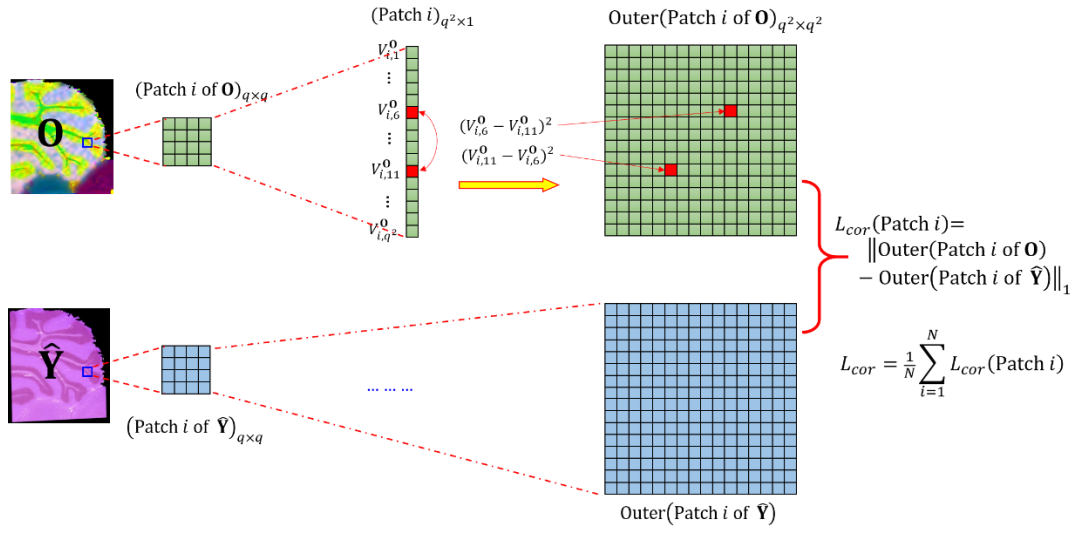


Figure S7. The calculation of \mathcal{L}_{cor} .

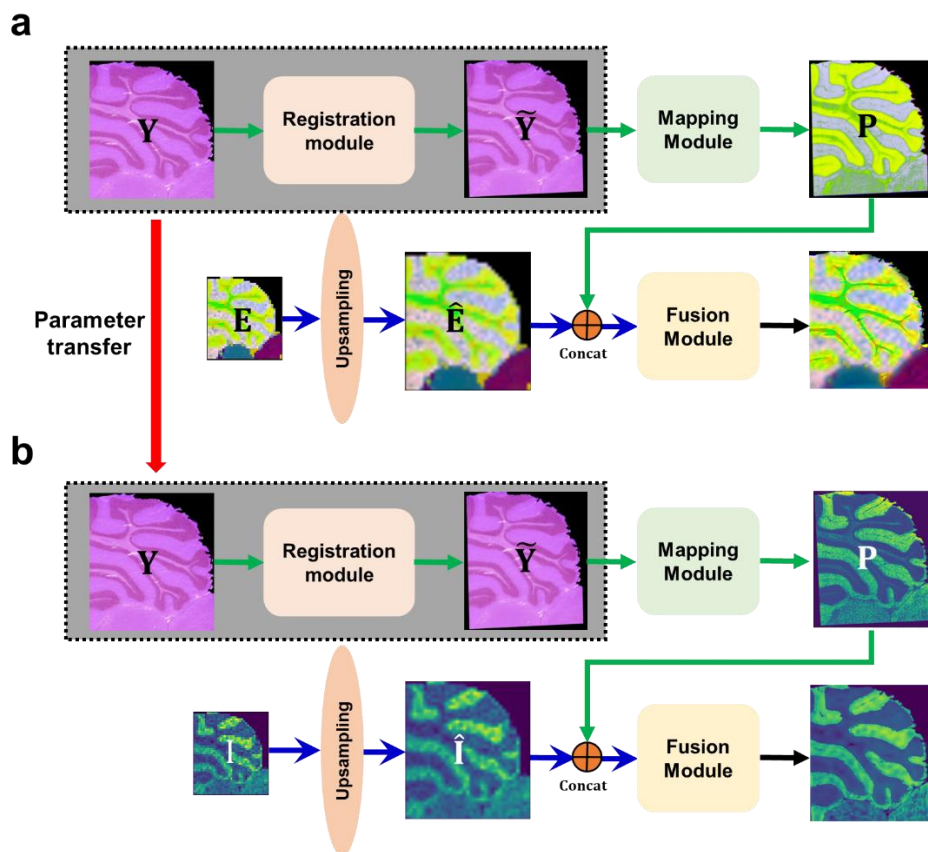


Figure S8. DeepFERE model for enhancing embedding data and single ion image. (a) DeepFERE for embedding data; (b) DeepFERE for single ion image.

Material S1. UMAP dimension reduction

Recently, dimensionality reduction is often used to reduce high-dimensional MSI data to two or three components for hyperspectral visualization while capturing the complete feature space. Uniform manifold approximation and projection (UMAP), as a nonlinear dimensionality reduction method, can reflect the molecular trends present in an entire tissue sample, which has shown its strong visualization capability in MSI data. Following the previous research³, we used UMAP to project the pixel-wise feature from original high-dimensional feature space to three-dimensional embedding space for visualization:

$$E_{M \times N \times 3} = \text{UMAP}(X_{M \times N \times H})$$

where $X_{M \times N \times H}$ is the original MSI data with H -dimensional data, and $E_{M \times N \times 3}$ is the embedding data with 3-dimensional data, the UMAP is achieved using python package (<https://pypi.org/project/umap-learn/0.1.5/>).

Material S2. Detailed of comparison methods

Aside from the proposed method, two baseline methods for high-resolution reconstruction of MSI data are considered: internal information-based interpolation method and referenced-based image fusion method. These baselines are described below.

Bicubic interpolation. Bicubic interpolation assumes the imputed pixel in MSI data has a strong correlation with the neighbor pixels, and they are obtained by calculating the weighted average of the nearest sixteen neighbor pixels. The detailed of bicubic interpolation can be found in Keys's work⁴.

Multi-modal fusion. Image fusion assumes there is much redundancy in the HR MSI and HR H&E image, so that the imputed pixel in LR MSI can be predicted using HR H&E image. The detailed of feature extraction and regression model construction can be found in Plas's work¹.

Material S3. Detailed of Ablation study

(1) Removal of the prediction loss L_{pre} . In this case, DeepFERE fails to capture the structural information of the H&E image. The removal of L_{pre} invalidates the registration module and the mapping module (Figure S5a), leading to inconsistency between \mathbf{P} and LR-MSI \mathbf{E} . Due to the removal, the registration module produces a uniform image of $\tilde{\mathbf{Y}}$ and forces L_{cor} to become a smooth regularization item.

(2) Removal of the correlation loss L_{cor} . The fine-structural information of H&E image $\tilde{\mathbf{Y}}$ cannot be fused into the HR-reconstructed MSI \mathbf{O} following the removal of correlation loss, leading to blurred ventricular region (Figure S5b). The result indicated that the fusion module fails to extract the fine-structural information of the H&E image.

(3) Removal of the reconstruction loss L_{rec} . If L_{rec} is removed from the model, the DeepFERE method tends to preserve the structural information of H&E image, but lose the intensity information of MSI (Figure S5c). The result demonstrated the fusion module fails to extract the intensity information from MSI data following the removal of L_{rec} .

Material S4. Potential solution to address overfitting

The potential solution to address the issue of overfitting as follows:

- (1) Conduct image reconstruction using the DeepFERE method (first round).
- (2) Identify and mask suspicious overfitted patches (e.g., morphology dissimilar subregion between H&E image and low-resolution MSI data) in the HR H&E image.
- (3) Second reconstruction round is conducted by using the H&E image with masked patches and the low-resolution MSI data, where \mathcal{L}_{cor} is not updated in masked region.
- (4) For the selected patches, compare the HR-enhanced MSI data before and after the masking procedure (i.e. compare results from the first and second round). If the difference between the first and second round is significant (e.g., $\text{MSE} > 0.05$), the selected patches are considered overfitted.
- (5) If the difference in Step 4 is not significant, the reconstruction results from the first round (Step 1) is accepted as the final reconstruction result. On the other hand, if the difference in Step 4 is significant, the reconstruction results from the second round (Step 3) is considered as the final reconstruction result, or the overfitted patches may be recalculated by introducing additional information.

Material S5. Detailed of MSI data preprocessing

Data preprocessing for raw MSI data is performed as follows:

Step 1: Spectral alignment. A statistical regression-based approach from He *et al.*⁵ is used to perform alignment and correct the random mass shifts (tolerance is set to 5 ppm) between each pixel and the referenced pixel (e.g., the first pixel).

Step 2: Peak detection. A feature selection approach is used to convert the mass spectrum to a peak list. Here, the detected peak must meet these two conditions: (1) the intensity of this peak is larger than twice of the noise peak intensity which is determined by MAD estimation; and (2) the intensity of this peak is a local maximum within the window size of 20 ppm.

Step 3: Peak binning. A peak binning algorithm from Gibb *et al.*⁶ is used to align the peaks into discrete bins, and equalize the m/z values of similar peaks in all pixels.

Step 4: Peak filtering. The uninformative peak is removed if the occurrence probability is less than 0.5%.

Step 5: Peak List pooling. We pool peak lists of all pixels to a global peak list, and set the intensities of imputation peaks to zero.

Here, the spectral alignment, peak detection and peak binning are performed using “MALDIquant”⁵ of R package, and the peak filtering and peak list pooling are performed using in-house python scripts.

Material S6. Detailed of Quantitative evaluation

Two metrics from grey-level co-occurrence matrix (GLCM) are used to performance evaluation for different high-resolution reconstruction methods.

GLCM-based correlation score. The GLCM based correlation score⁷ is used to evaluate the similarity between generated HR MSI and original LR MSI as follows:

$$p_{h,k} = \frac{m_{h,k}}{\sum_h \sum_k m_{h,k}} \quad (1)$$

where $p_{h,k}$ is the probability of each element of GLCM, $m_{h,k}$ is the number of pairs of gray-level h and k , and $h, k = 1, 2, \dots, 256$. In this study, four directions $\theta = 0^\circ, 45^\circ, 90^\circ, 135^\circ$ is considered, and on each direction, correlation statistic is applied to generate the feature vector of GLCM:

$$COR\ score = \frac{\sum_h \sum_k hkp_{h,k} - \mu_x \mu_y}{\sigma_x \sigma_y} \quad (2)$$

where $\mu_x, \mu_y, \sigma_x, \sigma_y$ represent average and Variance of p_h and p_k . Then, the GLCM-based correlation score is obtained through computing the Pearson correlation coefficient between the COR score of different methods. Larger GLCM-based correlation score means the method can better preserve the structure of the original data.

Out-of-sample prediction accuracy. Out-of-sample prediction accuracy is obtained by computing the mean square error (MSE) between predicted masked patch and true patch. Here, the predicted patch obtained from the model trained on the complete LR MSI and HR H&E image is regarded as true patches. It can be computed as follows:

$$MSE = \sum_{i=1}^M \sum_{j=1}^N \left\| \hat{X}_{i,j}^{pre} - \hat{X}_{i,j}^{true} \right\|_2 \quad (3)$$

where M and N are the high and width of the masked patch. In this study, we random selected ten patches, and the average of MSE error as the final result.

References

1. Van de Plas, R., Yang, J., Spraggins, J. & Caprioli, R. M. Image fusion of mass spectrometry and microscopy: a multimodality paradigm for molecular tissue mapping. *Nat. Methods* **12**(4), 366–372 (2015).
2. Inglese, P. et al. Deep learning and 3D-DESI imaging reveal the hidden metabolic heterogeneity of cancer. *Chem. Sci.* **8**(5), 3500-3511 (2017).
3. Smets, T., De Keyser, T., Tousseyn, T., Waelkens, E. & De Moor, B. Correspondence-Aware Manifold Learning for Microscopic and Spatial Omics Imaging: A Novel Data Fusion Method Bringing Mass Spectrometry Imaging to a Cellular Resolution. *Anal. Chem.* **93**(7), 3452-3460 (2021).
4. Keys R. Cubic convolution interpolation for digital image processing. *IEEE. T. Signal Proces* **29**(6), 1153-1160 (1981).
5. He, Q. P., Wang, J., Mobley, J. A., Richman, J & Grizzle, W. E. Self-calibrated warping for mass spectra alignment. *Cancer Inform* **10**, 65-82 (2011).
6. Gibb, S & Strimmer, K. MALDIquant: a versatile R package for the analysis of mass spectrometry data. *Bioinformatics* **28**, 2270-2271 (2012).
7. Haralick, R. M.; Shanmugan, K & Dinstein, I. Textural features for image classification. *IEEE. T. Syst. Man. Cybern* **SMC-3**(6), 610-621 (1973).